ChemComm

Is surface modification effective to stabilize high-voltage cycling for layered P2-$Na_{2/3}Ni_{1/3}Mn_{2/3}O_2$ cathode?

Journal:	*ChemComm*
Manuscript ID	CC-COM-06-2024-002819.R1
Article Type:	Communication

ChemComm

COMMUNICATION

Is surface modification effective to stabilize high-voltage cycling for layered P2-$Na_{2/3}Ni_{1/3}Mn_{2/3}O_2$ cathode?

Received 00th January 20xx,
Accepted 00th January 20xx

DOI: 10.1039/x0xx00000x

Fangzhou Niu,[a] Linna Qiao,[b] Heran Huang,[b] Elninoh A. Odero,[a] Guangwen Zhou,[bc] and Hao Liu*[ab]

Layered transition metal oxides (TMOs), like the P2-type $Na_{2/3}Ni_{1/3}Mn_{2/3}O_2$, are promising cathodes for sodium-ion batteries but suffer rapid capacity degradation at high voltages. Surface engineering is a popular strategy to modify the high-voltage stability of cathode materials, yet its efficacy for sodium layered TMOs remains elusive, especially given the deleterious layer-gliding phase transition during high-voltage operation. Here, we examined the effect of surface coatings on the high-voltage cycling stability of $Na_{2/3}Ni_{1/3}Mn_{2/3}O_2$, finding that they suppress high-voltage polarization but do not significantly affect capacity retention, which is mainly impacted by bulk structure degradation. Hence, surface engineering must be complemented with bulk structure modification to stabilize high-voltage cycling.

Sodium-ion batteries (SIBs) are promising candidates for large-scale energy storage applications due to the high abundance of Na on Earth. Among various cathode materials for SIBs, layered TMOs have garnered increasing attention in recent years due to their tunable chemical composition using earth-abundant elements and their high reduction potential for realizing high energy density electrodes. TMOs consist of slabs of close-packed transition metal and oxide ions, where the inter-slab space allows for the Na ion intercalation. The stacking sequence between the TMO slabs is broadly classified into the P-type (prismatic coordination for Na ions) and the O-type (octahedral coordination for Na) structures[1], which can be interchanged through a glide of the transition metal oxide slabs. The stability of the O-type vs the P-type structure is dependent on the composition of the transition metal and Na ions and can be described by the "cationic potential"[2]. In general, the P-type phase is stabilized for an intermediate Na concentration while the O-type phase is favored at low and high Na concentrations. In the Ni and Mn-based $Na_xNi_yMn_{1-y}O_2$, the phase transition between the P- and O-type phases is triggered at $x < 1/3$ and corresponds to a high voltage plateau (> 4 V Na^+/Na^0) with the nominal Ni^{4+}/Ni^{3+} redox reaction[3–6]. However, this high-voltage P-to-O phase transition is not fully reversible and results in an increased voltage polarization and the eventual demise of the high-voltage plateau after a few cycles[7]. As a result, nearly 1/3 Na per formula unit of Na_xTMO_2 must remain in the structure at the end of charge to maintain the P-type structure for reversible Na ion (de)intercalation, which significantly limits its reversible capacity. Recent mechanistic studies have revealed buckling and kinking[7,8] and exfoliation[9] of the TMO slabs following repeated P2-O2 phase transitions and oxygen redox and irreversible oxygen loss during charge of the high-voltage plateau[10,11]. Mitigation of these degradation reactions is necessary to enable the reversible cycling in the high voltage regime to develop high energy density cathodes.

Surface modification is a common strategy to improve the stability of cathode materials at high voltage. However, previous reports on surface-coated $Na_{2/3}Ni_{1/3}Mn_{2/3}O_2$ have yielded varying results: surface coating by Al_2O_3 using atomic layer deposition (ALD) shows a suppressed exfoliation at the particle surface and a stabilized cathode-electrolyte interface with no significant difference in the capacity degradation rate between the coated and non-coated electrode[12], whereas Al_2O_3 coating by a wet-chemical method shows a significant improvement in capacity retention and suppression of the voltage polarization [9]. Different from ALD, the wet chemical coating approach implemented a high-temperature annealing of the as-coated particles, which could readily lead to the inward diffusion of surface Al into the particle subsurface and interior, effectively doping the particles. This raises the question of whether surface modification alone is sufficient to mitigate the high-voltage degradation. Here, we adopted

[a] *Department of Chemistry, Binghamton University, Binghamton, New York 13902, United States*
[b] *Materials Science and Engineering, Binghamton University, Binghamton, New York 13902, United States*
[c] *Department of Mechanical Engineering, Binghamton University, Binghamton, New York 13902, United States.*
† Footnotes relating to the title and/or authors should appear here.
Supplementary Information available: [Methods, Figures S1-7, Tables S1-4]. See DOI: 10.1039/x0xx00000x

$Na_{2/3}Ni_{1/3}Mn_{2/3}O_2$ as the model P2 layered TMO cathode to interrogate the efficacy of surface coating on suppressing the high-voltage degradation.

A solid-state method[13] was used to synthesize P2-$Na_{2/3}Ni_{1/3}Mn_{2/3}O_2$ with a minor NiO impurity phase (**Fig. S1**). The $Na_{2/3}Ni_{1/3}Mn_{2/3}O_2$ powder was coated by Al_2O_3 using a wet chemical method, which mimics the reaction in atomic layer deposition to conformally coat the cathode particles[14]. The Al_2O_3-coated $Na_{2/3}Ni_{1/3}Mn_{2/3}O_2$ powder was vacuum-dried overnight at 80 °C (denoted as Al-NaNMO-80), and was subsequently annealed in air for 3 hrs at 300, 400, and 500 °C, which is denoted as Al-NaNMO-300, Al-NaNMO-400, and Al-NaNMO-500, respectively. The coating and annealing steps did not introduce significant changes to the bulk crystal structure of $Na_{2/3}Ni_{1/3}Mn_{2/3}O_2$ (**Fig. S2** and **Table S1**). High-angle annual dark field (HAADF) energy dispersive spectroscopy (EDS) mapping of an Al-NaNMO-400 particle shows the uniform distribution of Al, with 0.7 % molar ratio of Al to all transition metal ions (**Fig. 1**a-f, **Table S2**). The EDS mapping shows the uniform distribution of Al on an Al-NaNMO-400 particle, with the molar ratio of Al to all transition metal ions (Ni and Mn) corresponding to 0.7%. The high-resolution transmission electron microscopy (HRTEM) image of the Al-NaNMO-400 sample reveals a 1.5-nm thick layer on the particle surface (**Fig. 1**g), which is attributed to the Al_2O_3 coating. In contrast, a bare surface is observed for the pristine sample (**Fig. 1**h). This demonstrates the successful coating of Al_2O_3 on the $Na_{2/3}Ni_{1/3}Mn_{2/3}O_2$ particles.

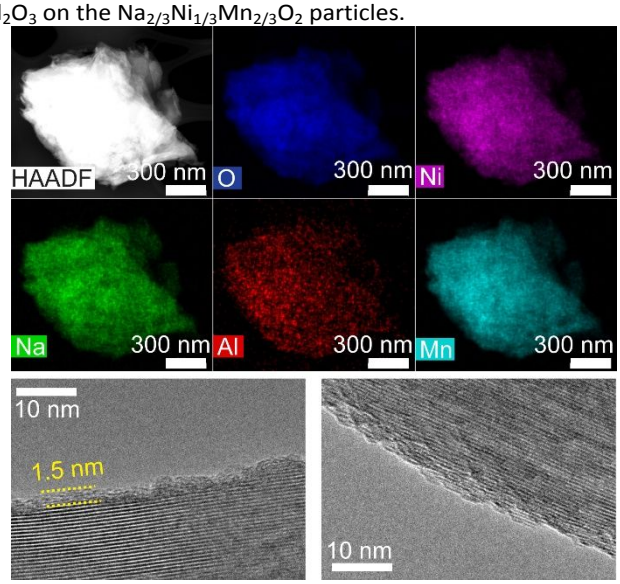

Fig. 1. (a) HADDF image and (b-f) corresponding EDS mapping of an Al-NaNMO-400 particle. (g) HRTEM image of an Al-NaNMO-400 particle revealing a thin amorphous layer on the surface. (h) HRTEM image obtained for a pristine particle, exhibiting a bare surface.

X-ray photoelectron spectroscopy (XPS) was used to interrogate the effect of annealing on the surface chemistry of the coated $Na_{2/3}Ni_{1/3}Mn_{2/3}O_2$ samples (**Fig. S3, Table S3-4**). As the annealing temperature increases from 80 °C to 500 °C, there is no significant shift in the Ni $3p_{3/2}$ peak, which indicates the preservation of Ni^{2+} on the particle surface. Peak fitting analysis shows a monotonic decrease of the Al 2p to Ni 3p peak area ratio from 0.63 to 0.30 with increasing annealing temperature. This corresponds to a decrease of the relative Al composition on the particle surface with increasing annealing temperature, which is attributed to the diffusion of surface Al into the particle interior at higher annealing temperatures, a phenomenon previously observed in coated particles following high-temperature annealing[15].

The effect of surface coating on the high-voltage degradation was examined by galvanostatic cycling in the voltage window of 2.5 – 4.5 V at C/20 (1 C corresponds to 260 mA/g) (**Fig. 2**a-e). As expected, the pristine $Na_{2/3}Ni_{1/3}Mn_{2/3}O_2$ sample (**Fig. 2**a) shows a well-defined voltage plateau at 4.2 V and 4.1 V on the first charge and discharge, respectively. As the cycle number increases, an increased voltage polarization is observed for both the charge and discharge plateau. This increased voltage polarization is evident in the differential capacity (dQ/dV) vs voltage plot (**Fig. 2**f), where the charge (discharge) peak shifts to higher (lower) voltages with increasing cycle number. For the coated samples, increased voltage polarization with cycle number is also observed for the high-voltage plateau (**Fig. 2**b-e and g-j). To quantify the voltage polarization, the difference in the position of the dQ/dV peak maximum on discharge and the equilibrium potential determined by the galvanostatic intermittent titration technique measurement (**Fig. S4**). For the pristine $Na_{2/3}Ni_{1/3}Mn_{2/3}O_2$ sample, the voltage polarization increases drastically from 0.05 V for the 1st cycle to 0.4 V for the 10th cycle (**Fig. 3**a), whereas all Al_2O_3-coated $Na_{2/3}Ni_{1/3}Mn_{2/3}O_2$ samples show a suppressed voltage polarization with the smallest voltage polarization observed for the Al-NaNMO-400 sample (0.1 V for the 10th cycle). This demonstrates surface modification as an effective strategy to suppress the high-voltage polarization. Nonetheless, none of the Al_2O_3-coated $Na_{2/3}Ni_{1/3}Mn_{2/3}O_2$ samples shows any improvement in capacity retention (**Fig. 3**b, **Fig. S5**). Both the pristine and Al-NaNMO-400 show similar rate capability (**Fig. S6**).

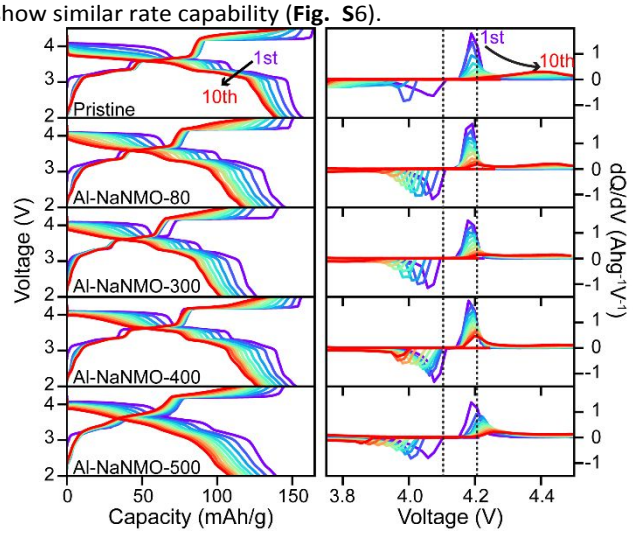

Fig. 2. (a-e) Galvanostatic charge and discharge voltage profiles and (f-j) the differential capacity plots for the pristine, Al-NaNMO-80, Al-NaNMO-300, Al-NaNMO-400, and Al-NaNMO-500 samples. All cells were cycled at a rate of 13 mA/g.

To interrogate the origin of the suppressed voltage polarization in the TMA-treated samples, electrochemical

impendence spectroscopy (EIS) measurement was performed for the pristine and Al-NaNMO-400 samples at the end of discharge. The Nyquite plot for the pristine electrode for the first cycle shows a single higher frequency (100 kHz to 10 Hz) semi-circle, which is ascribed to the surface film or the cathode electrolyte interphase (CEI) formed on the cathode particles, and a linear tail in the lower frequency range (< 10 Hz), which is ascribed to the Na-ion diffusion in the bulk electrode (**Fig. 4**a). From the third cycle, a semi-circle emerges in the intermediate frequency range (10 Hz to 0.1 Hz) and is ascribed to the charge transfer impedance[16]. The size of the middle-frequency semi-circle increases with cycle number, indicating the growing charge transfer impedance over cycles. Similar to the pristine electrode, the Al-NaNMO-400 electrode exhibits a single semi-circle in the first cycle with the appearance and growth of a second semi-circle in later cycles. An equivalent circuit model (**Fig. 4**b) encompassing the contact resistance (R_0), two interfacial impedances (R_{CEI}/CPE_{CEI} and R_{CT}/CPE_{CT}), and an open Warburg element (W_o) was used to fit the EIS data. As shown in **Fig. 4**b, the resistance of the CEI layer (R_{CEI}) grows from 200 Ω in the 1st cycle to 483 Ω in the 10th cycle for the pristine $Na_{2/3}Ni_{1/3}Mn_{2/3}O_2$ electrode and from 378 Ω in the 1st cycle to 562 Ω in the 10th cycle for the Al-NaNMO-400 electrode. In contrast, the charge transfer resistance (R_{CT}) grows from 432 Ω in the 3rd cycle to 4422 Ω in the 10th cycle for the pristine $Na_{2/3}Ni_{1/3}Mn_{2/3}O_2$ electrode and from 503 Ω in the 3rd cycle to 2691 Ω in the 10th cycle for the Al-NaNMO-400 electrode. An accelerated R_{CT} growth is observed for the pristine $Na_{2/3}Ni_{1/3}Mn_{2/3}O_2$ electrode from the 8th cycle, after which the R_{CT} takes over that of the Al-NaNMO-400 electrode. This diverging trend in the R_{CT} is consistent with the larger voltage polarization observed for the pristine electrode in **Fig. 3**a.

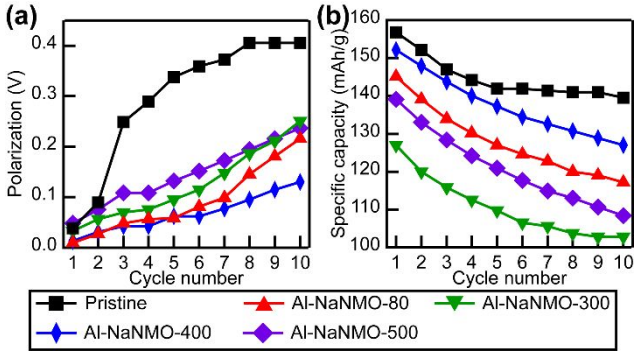

Fig. 3. (a) Voltage polarization for the high voltage plateau during discharge. (b) Specific discharge capacity and Coulombic efficiency of the pristine, Al-NaNMO-80, Al-NaNMO-300, Al-NaNMO-400, and Al-NaNMO-500 electrodes during the first 10 cycles at C/20 (13 mA/g) between 2.5 and 4.5 V.

Since the charge transfer process is coupled with the P2-O2 phase transition, we probed the evolution of the P2-O2 phase transition over cycles using *operando* X-ray diffraction (XRD), which was performed for the pristine and Al-NaNMO-400 samples during the first 8 charge-discharge cycles in the voltage range of 3.75 – 4.5 V (**Fig. 5**a and b). For the pristine sample (**Fig. 5**a), the continuous shift of the P2 phase (002) reflection to lower 2θ angles corresponds to the solid-solution reaction before the two-phase reaction at the 4.2 V plateau[17], where the (002) reflection for the O2 phase starts to grow at the expense of the P2 phase [17–20]. Upon discharge, the P2 phase (002) reflection re-emerges and grows at the expense of the O2 phase. Similar observations are made for the subsequent cycles except that the maximum intensity of the (002) reflection of the O2 phase decreases over cycles, which is captured by the Pawley fitting result (**Fig. S7**a). This suggests that less O2 phase was formed at the end of charge in later cycles, which is consistent with the observed capacity loss over cycles in the electrochemical cycling result (**Fig. S8**). A similar observation is made for the *operando* XRD data for the Al-NaNMO-400 sample (**Fig. 5**b). The lattice parameters of the P2 and O2 phases are effectively constant throughout the repeated P2-O2 phase transition cycles (**Figs. S7**b and c) for both the pristine and Al-NaNMO-400 samples. No significant differences in the lattice parameters are observed between the two samples. This shows that the surface coating does not significantly affect the bulk crystal structure evolution during high-voltage cycling. Substantial morphological changes are observed for both the cycled pristine and Al-NaNMO-400 samples. (**Fig. S9**)

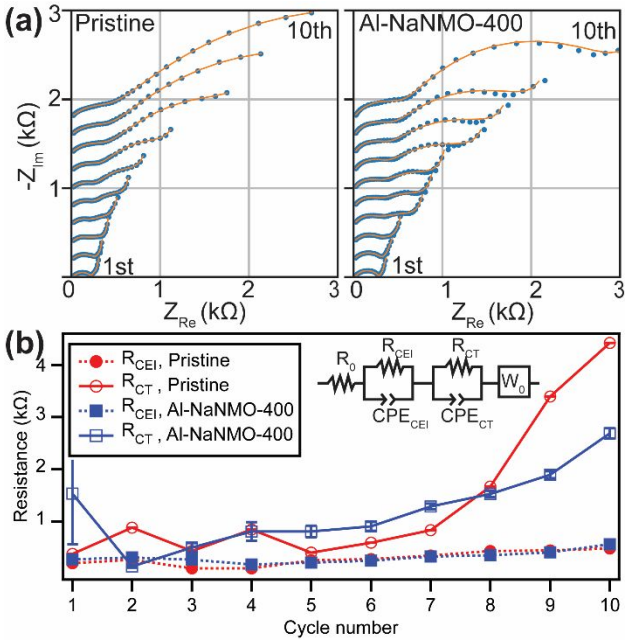

Fig. 4. (a) Nyquist plots of the EIS measured for the pristine $Na_{2/3}Ni_{1/2}Mn_{2/3}O_2$ and Al-NaNMO-400 electrodes at the end of discharge of the galvanostatic cycling between 3.75V and 4.5V at C/20 (13 mA/g). (b) Resistance of the cathode-electrolyte interface (R_{CEI}) and the charge transfer resistance (R_{CT}) obtained by the equivalent circuit modeling of the EIS data measured over cycles. The equivalent circuit model is shown as the inset. CPE corresponds to the const phase element.

In performing the Pawley fitting, an anisotropic broadening model was used to account for the *hkl*-dependent peak width, where the peak profiles for the (*h*00) and (00*l*) reflections were refined independently from the other reflections using an anisotropic microstrain broadening model. For both the <*h*00> and <00*l*> lattice directions, the microstrain increases substantially with cycle numbers (**Fig. 5**c and d), which indicates growing structure disorder in the material. This structure disorder is attributed to the buckling and kinking of the TMO layers developed after repeated P2-O2 phase transition[7,8]. However, both samples show comparable increase in the microstrain at the 8th cycle, which indicates no significant

impact of surface modification on the bulk structure degradation over repeated high-voltage P2-O2 phase transitions.

Unlike previous reports of improved capacity retention for the surface modified $Na_{2/3}Ni_{1/3}Mn_{2/3}O_2$[9,12,21], the suppressed voltage polarization and charge transfer impedance growth found for Al-NaNMO-400 in the present work does not concur with improved capacity retention. It is worth noting that the capacity retention of our pristine sample is similar to the Al_2O_3-coated electrode by ALD[12]. Al_2O_3 coating using the wet chemical method likely induces bulk doping given the slopy voltage profile[9] , which is typically achieved by bulk substitution[22], and extended thermal treatment, promoting bulk doping [23]. Therefore, suppressing the growth of charge transfer impedance alone is not sufficient to increase capacity retention. In contrast to the efficacy of surface modification in stabilizing the high-voltage cycling of lithium layered TMO[24,25], which does not suffer from the layer-gliding phase transition, surface modification has little impact on the high-voltage degradation for the sodium layered TMO, which is predominated by bulk structural disorder as demonstrated in the present study. Thefore, future work to improve the high-voltage stability of sodium layered TMO should focus on suppressing the layer-gliding phase transition.

This research is supported by the startup funding of Binghamton University and the National Science Foundation CBET-2144296 and CBET-2028722.

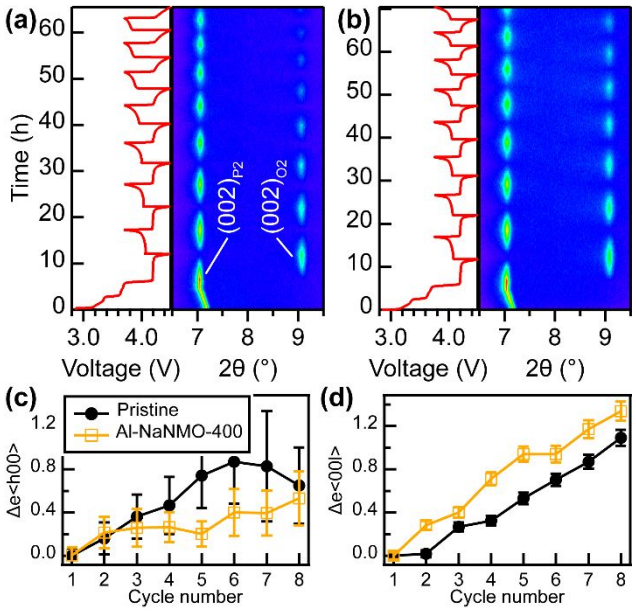

Fig. 5. (a) Long duration Operando-XRD of Pristine and the voltage profile. (b) Long duration Operando-XRD of Al-NaNMO-400 and the voltage profile. Incremental microstrain along (c) <h00> and (d) <00l> directions. The incremental microstrain is deduced by subtracting the microstrain at the beginning of first charge from the refined microstrain values.

Data availability

The data supporting this article have been included as part of the Supplementary Information.

Conflicts of interest

There are no conflicts to declare.

Notes and references

1 C. Delmas, C. Fouassier and P. Hagenmuller, *Physica B+C*, 1980, **99**, 81–85.
2 2 C. Zhao, Q. Wang, Z. Yao, J. Wang, B. Sánchez-Lengeling, F. Ding, X. Qi, Y. Lu, X. Bai, B. Li, H. Li, A. Aspuru-Guzik, X. Huang, C. Delmas, M. Wagemaker, L. Chen and Y. S. Hu, *Science (1979)*, 2020, **370**, 708–712.
3 S. Komaba, N. Yabuuchi, T. Nakayama, A. Ogata, T. Ishikawa and I. Nakai, *Inorg Chem*, 2012, **51**, 6211–6220.
4 Z. Lu and J. R. Dahn, *J Electrochem Soc*, 2001, **148**, A1225.
5 J. Liu, C. Didier, M. Sale, N. Sharma, Z. Guo, V. K. Peterson and C. D. Ling, *J Mater Chem A Mater*, 2020, **8**, 21151–21162.
6 T. Risthaus, L. Chen, J. Wang, J. Li, D. Zhou, L. Zhang, D. Ning, X. Cao, X. Zhang, G. Schumacher, M. Winter, E. Paillard and J. Li, *Chemistry of Materials*, 2019, **31**, 5376–5383.
7 M. Jiang, G. Qian, X.-Z. Liao, Z. Ren, Q. Dong, D. Meng, G. Cui, S. Yuan, S.-J. Lee, T. Qin, X. Liu, Y. Shen, Y.-S. He, L. Chen, Y. Liu, L. Li and Z.-F. Ma, *Journal of Energy Chemistry*, 2022, **69**, 16–25.
8 Y. Li, X. Li, C. Du, H. Sun, Y. Zhang, Q. Liu, T. Yang, J. Zhao, C. Delmas, S. J. Harris, H. Chen, Q. Huang, Y. Tang, L. Zhang, T. Zhu and J. Huang, *ACS Energy Lett*, 2021, **6**, 3960–3969.
9 Y. Liu, X. Fang, A. Zhang, C. Shen, Q. Liu, H. A. Enaya and C. Zhou, *Nano Energy*, 2016, **27**, 27–34.
10 K. Dai, J. Mao, Z. Zhuo, Y. Feng, W. Mao, G. Ai, F. Pan, Y. de Chuang, G. Liu and W. Yang, *Nano Energy*, 2020, **74**, 104831.
11 Y. Zhang, M. Wu, J. Ma, G. Wei, Y. Ling, R. Zhang and Y. Huang, *ACS Cent Sci*, 2020, **6**, 232–240.
12 J. Alvarado, C. Ma, S. Wang, K. Nguyen, M. Kodur and Y. S. Meng, *ACS Appl Mater Interfaces*, 2017, **9**, 26518–26530.
13 G. Singh, N. Tapia-Ruiz, J. M. Lopez Del Amo, U. Maitra, J. W. Somerville, A. R. Armstrong, J. Martinez De Ilarduya, T. Rojo and P. G. Bruce, *Chemistry of Materials*, 2016, **28**, 5087–5094.
14 R. S. Negi, S. P. Culver, A. Mazilkin, T. Brezesinski and M. T. Elm, *ACS Appl Mater Interfaces*, 2020, **12**, 31392–31400.
15 D. S. Hall, M. Katharina, J. Slaughter, D. S. Wright and C. P. Grey, , DOI:10.1021/acs.chemmater.2c02580.
16 N. Andreu, D. Flahaut, R. Dedryvère, M. Minvielle, H. Martinez and D. Gonbeau, *ACS Appl Mater Interfaces*, 2015, **7**, 6629–6636.
17 M. Jiang, G. Qian, X. Z. Liao, Z. Ren, Q. Dong, D. Meng, G. Cui, S. Yuan, S. J. Lee, T. Qin, X. Liu, Y. Shen, Y. S. He, L. Chen, Y. Liu, L. Li and Z. F. Ma, *Journal of Energy Chemistry*, 2022, **69**, 16–25.
18 Y. H. Jung, A. S. Christiansen, R. E. Johnsen, P. Norby and D. K. Kim, *Adv Funct Mater*, 2015, **25**, 3227–3237.
19 X. Wu, G. L. Xu, G. Zhong, Z. Gong, M. J. McDonald, S. Zheng, R. Fu, Z. Chen, K. Amine and Y. Yang, *ACS Appl Mater Interfaces*, 2016, **8**, 22227–22237.
20 F. Tournadre, L. Croguennec, P. Willmann and C. Delmas, *J Solid State Chem*, 2004, **177**, 2803–2809.
21 J. H. Jo, J. U. Choi, A. Konarov, H. Yashiro, S. Yuan, L. Shi, Y. K. Sun and S. T. Myung, *Adv Funct Mater*, 2018, **28**, 1–11.
22 F. Xin, H. Zhou, Y. Zong, M. Zuba, Y. Chen, N. A. Chernova, J. Bai, B. Pei, A. Goel, J. Rana, F. Wang, K. An, L. F. J. Piper, G. Zhou and M. S. Whittingham, *ACS Energy Lett*, 2021, **6**, 1377–1382.
23 Y. Jin, H. Yu and X. Liang, *Appl Phys Rev*, 2021, **8**, 031301.

The data supporting this article have been included as part of the Supplementary Information.